International Journal of Cast Metals Research

ISSN: 1364-0461 (Print) 1743-1336 (Online) Journal homepage: http://www.tandfonline.com/loi/ycmr20

The transition from stable to metastable system and its relation with the ferrite halo extension in SG cast irons

Laura N. García, Fernando D. Carazo & Patricia M. Dardati

To cite this article: Laura N. García, Fernando D. Carazo & Patricia M. Dardati (2017): The transition from stable to metastable system and its relation with the ferrite halo extension in SG cast irons, International Journal of Cast Metals Research, DOI: 10.1080/13640461.2017.1408754

To link to this article: https://doi.org/10.1080/13640461.2017.1408754

Published online: 05 Dec 2017.

INTERNATIONAL JOURNAL OF CAST METALS RESEARCH, 2017
https://doi.org/10.1080/13640461.2017.1408754

Taylor & Francis
Taylor & Francis Group

The transition from stable to metastable system and its relation with the ferrite halo extension in SG cast irons

Laura N. García[a,b], Fernando D. Carazo[a,b] and Patricia M. Dardati[c]

[a]CONICET, Godoy Cruz 2290 (C1425FQB), CABA, Buenos Aires, Argentina; [b]Instituto de Mecánica Aplicada, Universidad Nacional de San Juan, San Juan, Argentina; [c]Facultad Regional Córdoba, Departamento de Ingeniería Mecánica, Universidad Tecnológica Nacional, Córdoba, Argentina

ABSTRACT

Microsegregations of alloying elements developed during solidification are known to affect solid state transformations in spheroidal graphite cast irons. However, no clear relation between them and the presence and extension of ferrite halos has been established until now. The aim of the present work is to expose how the microsegregations of Si, Mn and Cu influence in the transition from stable to metastable system during solid state transformations and how the extension of the ferrite halo is affected accordingly. The study was carried out on samples cast at a cooling rate of 20 K/min, which allowed the diffusion of carbon under equilibrium conditions.

ARTICLE HISTORY
Received 6 June 2017
Accepted 15 November 2017

KEYWORDS
Spheroidal graphite cast irons; ferrite halo; microsegregations; eutectoid critical temperatures

Introduction

Cast irons are alloys mainly composed of Fe, C and Si. This latter element avoids the formation of cementite since it acts as a graphite stabilizer and allows obtaining cast irons. Further, spheroidal graphite cast irons (from now on SG cast irons) refer to a subtype in which graphite adopts spheroidal shape by a nodulizing treatment. This particular characteristic reduces cutting effects and stress concentrations when compared to other cast irons [1].

In SG cast irons, graphite nodules are enveloped by ferrite halos and the resultant structure is termed as bull's-eye ferrite because of its bull's eye appearance, as shown in Figure 1. The rest of the microstructure consists of varying amounts of pearlite. Both ferrite and pearlite are originated during the transformation of the austenite enclosing the graphite nodules after the solidification step.

Moreover, some alloying elements are added in order to modify the percentage of the present phases and their mechanical properties accordingly. Among them Mn and Cu are the focus of this study, together with Si. These alloying elements redistribute during the solidification step: Si and Cu (graphitizing elements) tend to segregate toward the first-to-freeze zones and to the perinodular liquid, while Mn (carbide stabilizing element) tends to concentrate in the residual liquid, i.e. into the last-to-freeze zones, as revealed by Boeri in his PhD thesis [2]. In addition, Boeri studied the segregations of quenched and sand-cast samples by means of microprobe analysesand found them to be of the same magnitude. Thus, he concluded that the segregation profiles from solidification are inherited by austenite and that there is no diffusion of substitutional elements during solid state transformations for continuous cooling treatment.

The above mentioned fact supports the paraequilibrium concept adopted by Lacaze et al. [3] which allowed them to explain solid state transformations employing an isopleth Fe–C section with the the nominal weight percentage of Si of the alloy studied in that occasion. For the present work a 2.5wt-%Si isopleth section was represented by means of Thermo-Calc software [4], as shown in Figure 2(a). According to the authors, ferritic reaction can proceed only at temperatures below $T_{\alpha'}$ since carbon concentration gradient for diffusion through the ferrite, turns to positive values in that case. This temperature is determined by the intersection of the extrapolation of the austenite/ferrite boundary with the lowest limit of the three-phase ferrite/austenite/graphite field. Once the temperature of the alloy has reached the upper limit of the three-phase ferrite/austenite/graphite field, denoted by T°_{α}, ferrite could possibly nucleate but cannot grow since this would involve long range redistribution of substitutional elements between ferrite and austenite.

Concerning pearlitic reaction, Lacaze et al. [3] described it in an isopleth section like the one indicated

CONTACT Laura N. García lauranoelg@gmail.com

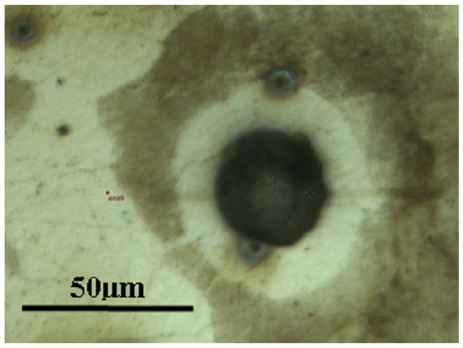

Figure 1. Bull's eye structure: graphite nodule enveloped by ferrite. The matrix of the alloy is pearlitic.

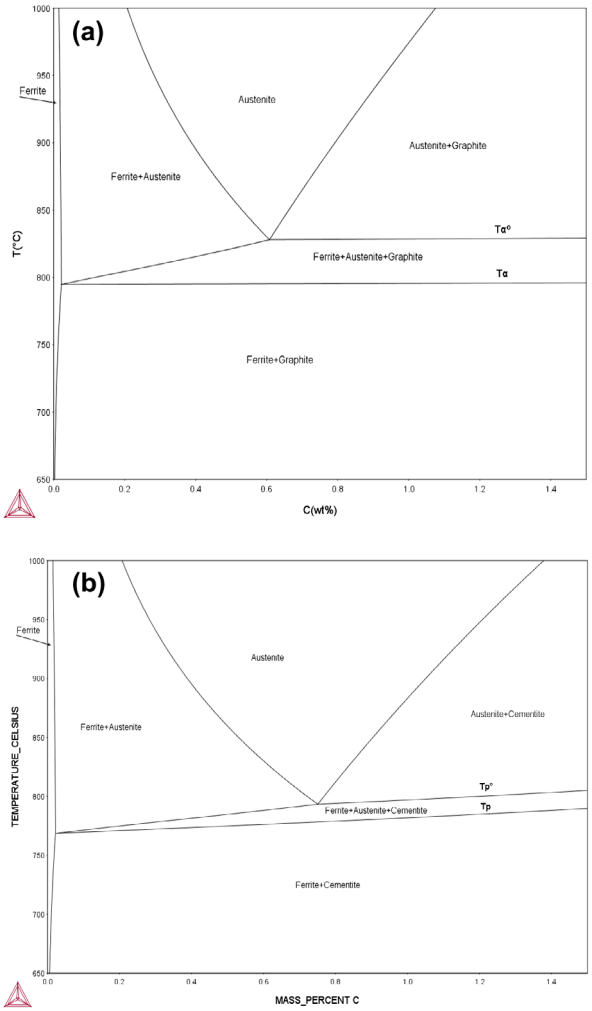

Figure 2. Isopleth sections of a FeCSi system for 2.5 wt-%Si as obtained by means of Thermo-Calc software: (a) stable system and (b) metastable system. Refer to the text for the definition of the specified temperatures.

in Figure 2(b). Thus, cementite could nucleate when the temperature of the alloy has reached T_p° (upper limit of the three-phase ferrite/austenite/cementite field), but cannot grow until it has reached T_p (intersection of the extrapolation of the austenite/ferrite boundary with the lowest limit of the three-phase ferrite/austenite/cementite field).

For similar cooling rates, ferrite and pearlite fractions mainly depend on the distribution of Si and alloying elements in the austenite inherited from the solidification [5]. Nevertheless, it is not yet understood how the extension of the ferrite halos is conditioned by these microsegregation profiles. To the best of the authors' knowledge, only Roviglione [6] has focused on trying to find a clear relation between these aspects. Roviglione inferred that the extension of the ferrite halos would be related to the pile up process of Si around the graphite nodules developed in the melt during the solidification process. The length of this accumulation is determined by the ratio between the diffusion coefficient of Si in the liquid and the rate at which the solid/liquid interface advances. The extension of the ferrite halos would be of the same order of this length.

In the present work, we investigate the role of Si, Mn and Cu contents in the transition from stable to metastable system, which would limit the growth of ferrite giving way to pearlite nucleation and growth –under equilibrium conditions, transition from stable to metastable eutectoid system refers to the step at which austenite stops its decomposition to ferrite plus graphite to give way to the pearlite nucleation and growth-. This approach casts light on the different extensions of the ferrite halos that can be found in SG cast irons. For this purpose, microprobe analyses were carried out for three different types of SG cast irons with varying percentages of Mn and Cu, and approximately the same percentage of Si. Later on, use was made of the critical temperature expressions developed by Gerval et al. [7], and subsequently improved by Gerval and Lacaze [8], to explore the behavior of local critical temperatures among different points of the matrix.

Experimental details

The compositions and classification of the three types of alloys employed are indicated in Table 1. In each case, the melt was obtained in a high-frequency induction furnace

Table 1. Compositions of the three employed SG cast irons [values in wt-%].

SG cast iron	C	Si	Mn	P	S	Cr	Cu	Sn	Mg	Al	CE
1. Ferritic	3.67	2.8	0.21	0.038	0.01	0.025	0.01	0.009	0.041	0.012	4.70
2. Pearlitic-ferritic	3.55	2.8	0.36	0.034	0.025	0.029	0.3	0.012	0.048	0.008	4.49
3. Pearlitic	3.58	2.72	0.5	0.02	0.01	0.031	0.82	0.017	0.049	0.013	4.49

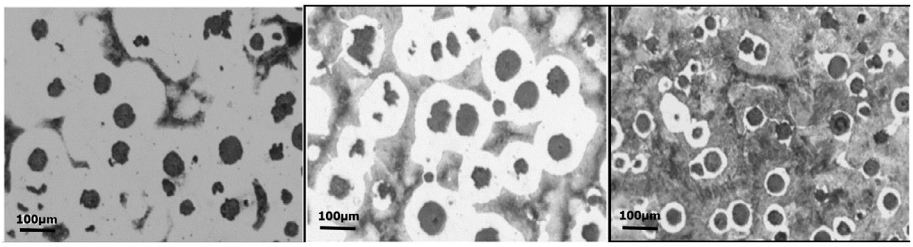

Figure 3. SG cast irons studied in the present work: (a) ferritic alloy, (b) pearlitic-ferritic alloy, and (c) pearlitic alloy. They were investigated with optical microscopy.

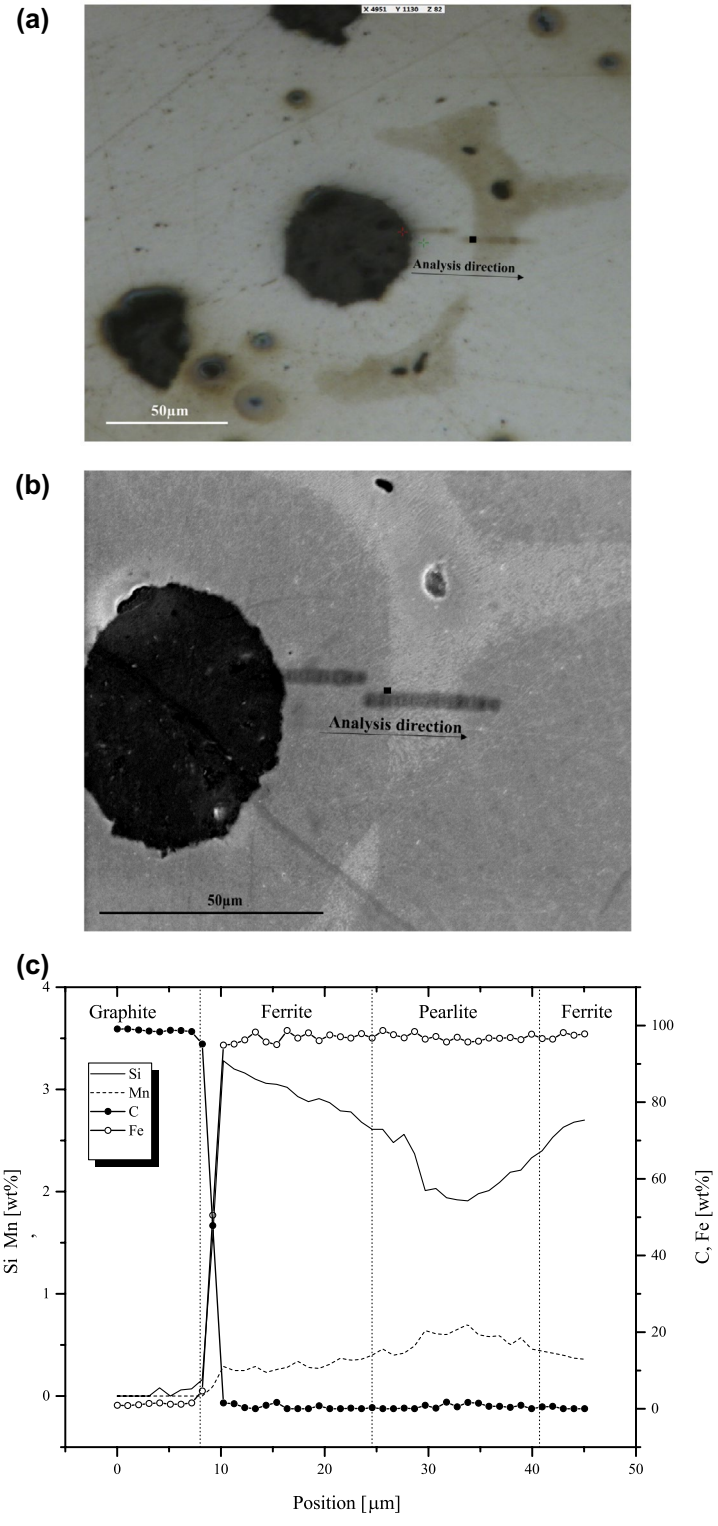

Figure 4. Microprobe analysis of a ferritic sample: (a) optical microscope image and (b) SE image. The position of the ferrite/pearlite interface is indicated with a full black square. The analysis directions are specified as well and (c) element's segregation profile.

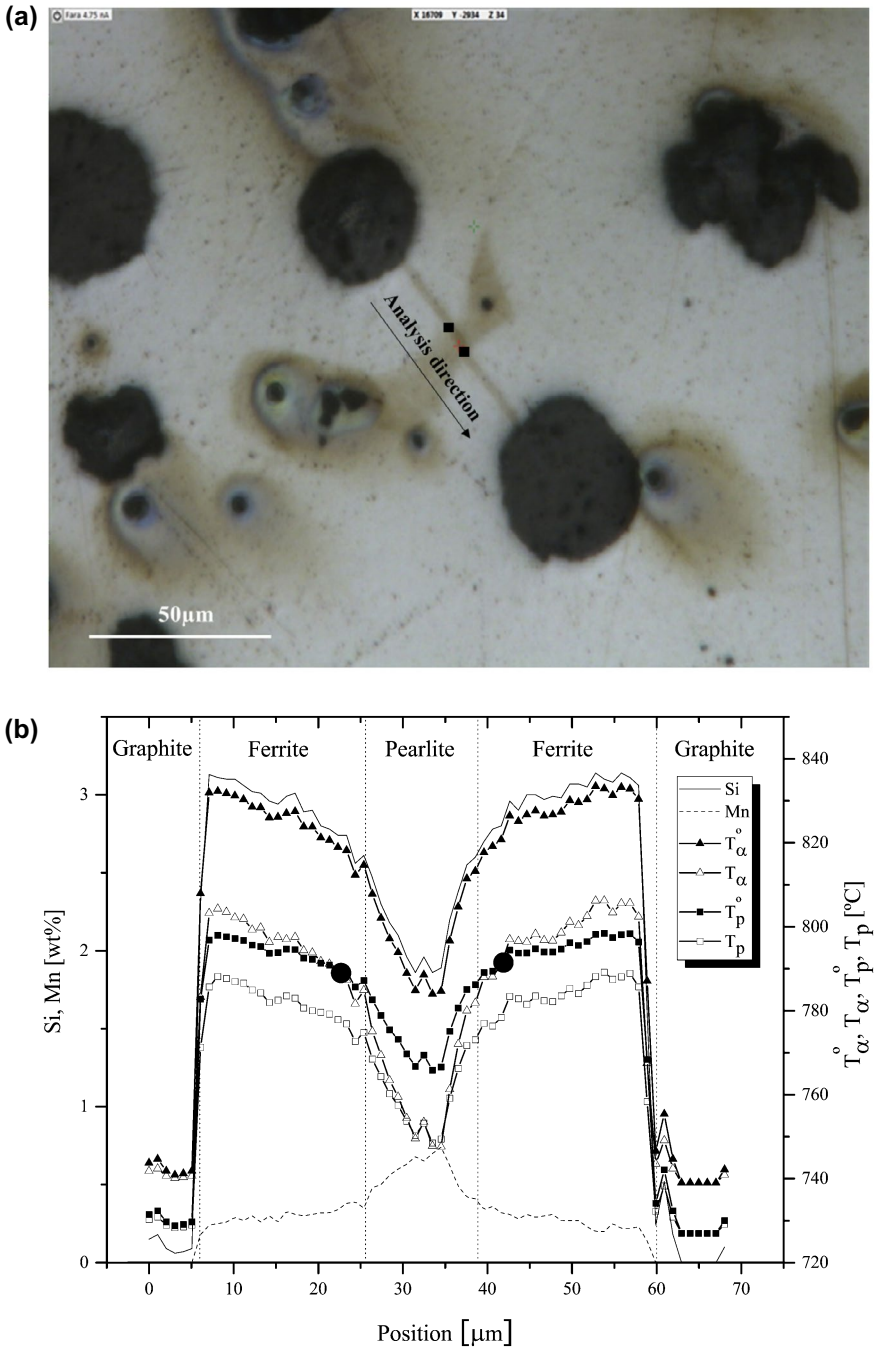

Figure 5. Ferritic sample: (a) optical image. The position of the ferrite/pearlite interface is indicated with a full black square. The analysis directions are specified as well and (b) critical temperature and compositional profiles. The intersection between T_α and T_p° is denotated with a full black circle.

with a capacity of 1500 kg. Different percentages of SAE 1010 scraps, retrieved SG cast iron, pig iron and charcoal were cast for this purpose. Ground graphite was added in order to set the C content, while Si_2Ca and FeSi were used for adjusting the silicon composition of the metal. Successively, the base metal was overheated to 1650 °C for 20 min, after what approximately 1.5wt-% of Fe–Si–Mg–Ce was used as nodulizing agent. The graphitization and inoculation processes were conducted using the sandwich method. In the reaction ladle, 0.7wt-% of fine FeSi (75wt-%Si) was added. Finally, the cast metal was poured into the cast ladle to fill Y-block shaped green sand moulds for obtaining 1-inch Y-blocks according to ASTM A536-84 [9]. For each alloy composition, two Y-blocks were cast at 20 K/min.

In a later step, one cylindrical specimen for each block was considered for mechanizing five metallographic samples. In total, 30 metallographic specimens were prepared by conventional polishing and etched with 5% nital. Through optical observations and making use

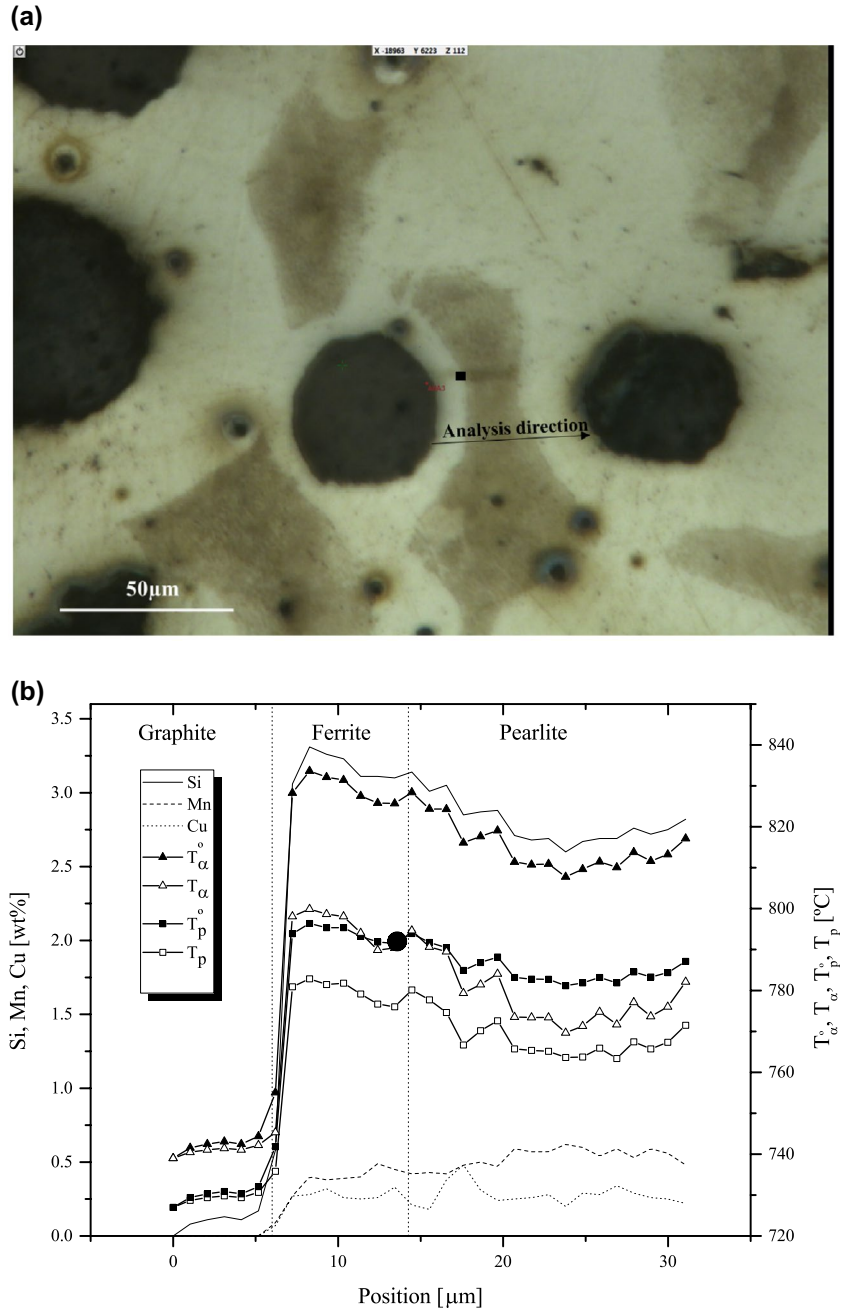

Figure 6. Pearlitic-ferritic sample: (a) optical image. The position of the ferrite/pearlite interface is indicated with a full black square. The analysis directions are specified as well and (b) critical temperature and compositional profiles. The intersection between T_{α} and T°_{p} is denotated with a full black circle.

of Material Plus software, it was possible to establish the percentage of the present phases and therefore to classify the alloys. An example of these optical observations is shown in Figure 3, where the alloys are classified into ferritic, pearlitic-ferritic and pearlitic samples.

Six of the 30 available metallographic samples were chosen for microprobe quantitative analyses: two ferritic, two pearlitic-ferritic and two pearlitic specimens. The following elements were examined: Si, Mn, Cu, Fe and C. Before conducting the study, it was necessary to polish the samples using 1 µm diamond paste. Further, they were etched with 3% nital so that their microstructure could be revealed.

The analyses were performed using a Cameca SX Five microprobe with an accelerating voltage of 20 kV and a beam current of 5 nA. The soft nital etch ensured that no errors were introduced in the measurements. The concentration of the elements was determined by difference with C and studied along straight lines going from the periphery of the graphite nodules, through the ferrite,

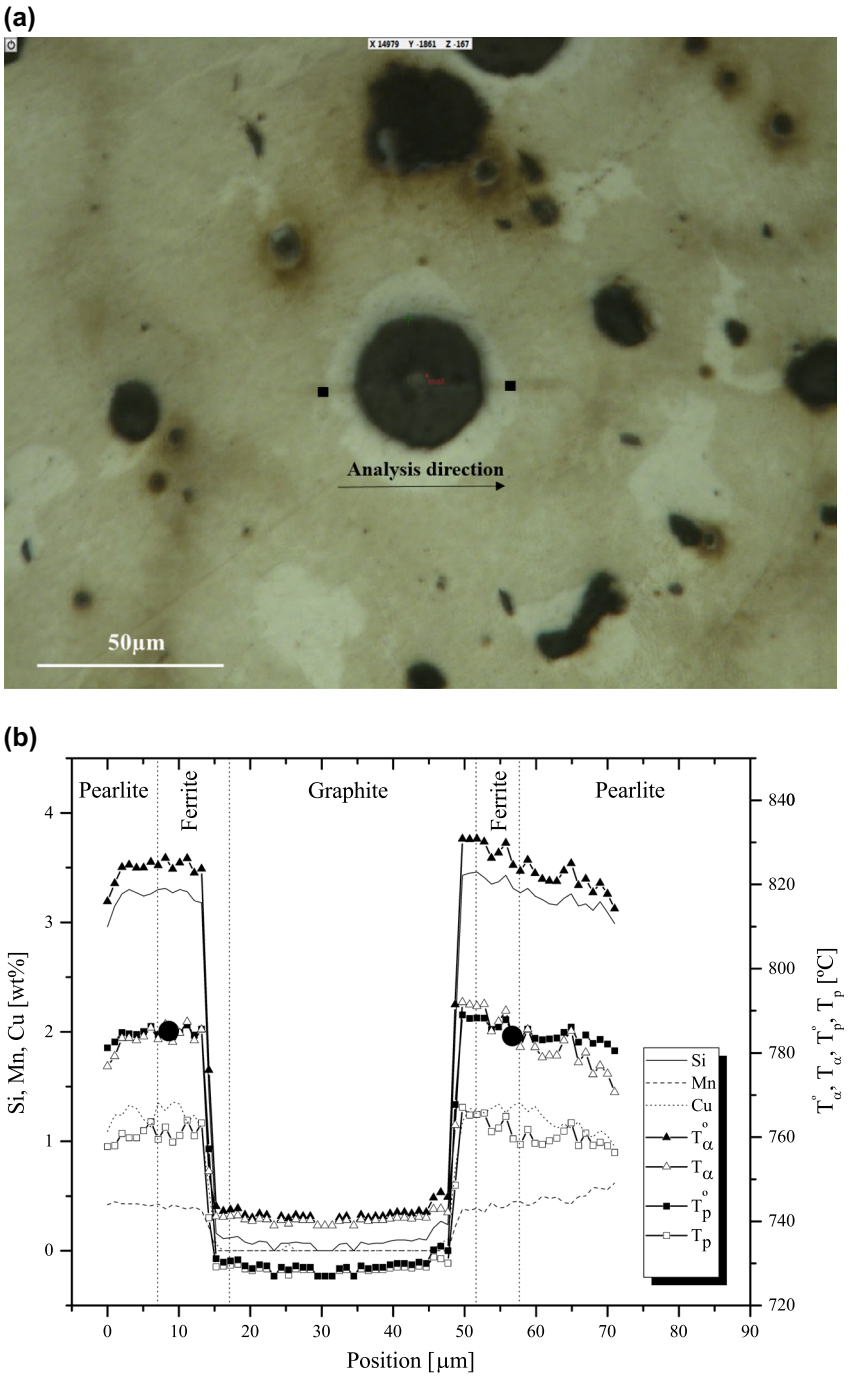

Figure 7. Pearlitic sample: (a) optical image. The position of the ferrite/pearlite interface is indicated with a full black square. The analysis directions are specified as well, (b) critical temperature and compositional profiles. the intersection between T_α and t_p° is denotated with a full black circle.

up to the pearlite. The size of the spot was between 0.2 and 0.5 µm and the quantitative analyses were achieved by examining points at 1 µm distance from each other. The incident beam left a distinguishable mark in each sample through the described path. Optical and secondary electron (SE) images were recorded. In total, forty profiles were registered. In the case of ferritic samples, the measured copper concentrations were lower than the detection limit of 500 ppm, as expected (Table 1).

An example of a ferritic studied sample is presented in Figure 4. In Figure 4(a) an optical image is displayed where the path left by the microprobe analysis can be recognized. Figure 4(b) corresponds to a SE image and the same path as in Figure 4(a) can be appreciated. In both images, the analysis direction is specified and the ferrite/perlite interface pointed with a full black square. Finally, the matching microsegregation profile is exposed in Figure 4(c) and it reflects the expected segregation

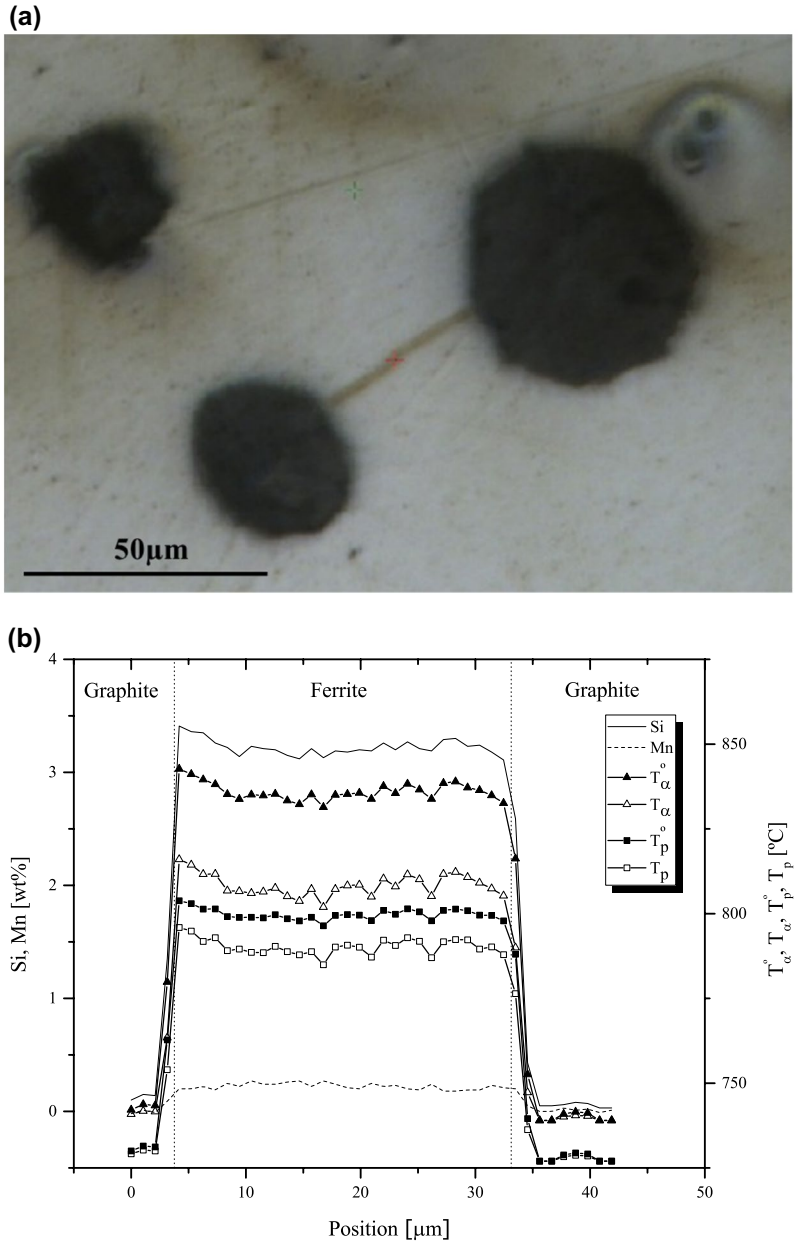

Figure 8. Ferritic sample: (a) optical image and (b) critical temperature and compositional profiles.

behaviors of the studied elements, i.e. Si goes to ferritic zones while Mn partitions to perlitic zones.

Results

After acquiring all the microsegregation profiles and assuming no partition of substitutional elements, use was made of the temperature expressions developed by Gerval and Lacaze [8] by means of Thermocalc software and Uhrenius data base. These equations are valid for SG cast irons with Si contents up to 3wt-% and for Mn and Cu contents up to 0.5wt-%. Nevertheless, they were employed even for those points overcoming these limits, as the main goal of this study was not to obtain the exact critical temperature patterns, but to understand their behavior through the examined paths.

One example of the studied paths for each of the considered alloys is provided in Figures 5–7. They also depict the corresponding segregation and critical temperature profiles. It can be noticed that T_{α} and T°_{p} converge in a point, which is marked out by a full black circle. This point is very close to the position of the ferrite/pearlite interface, especially for pearlitic alloys.

Additionally, the alloying elements' profiles do not present a compositional jump when going through the ferrite/pearlite interfaces, but they do present a slope change.

Apart from the previous cases, others were investigated. They are presented from Figures 8–11 and

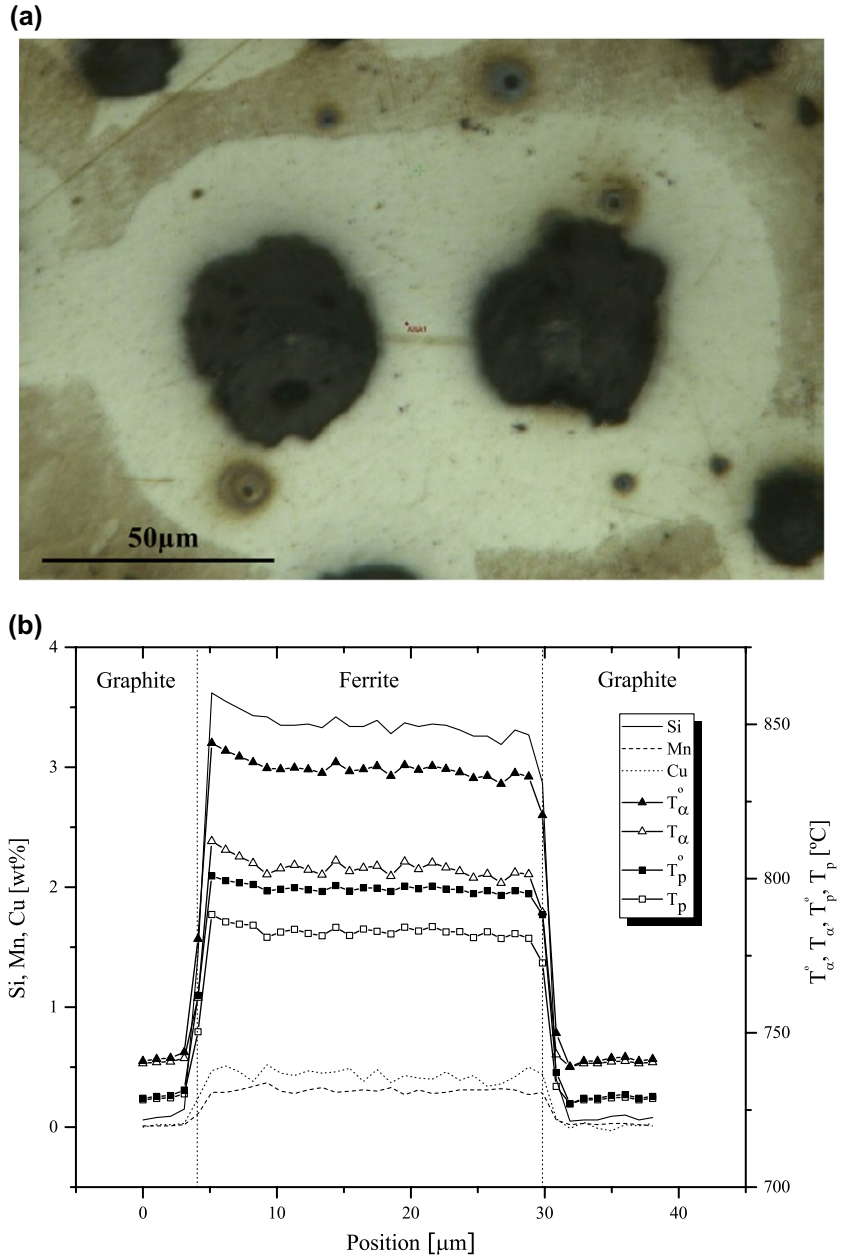

Figure 9. Pearlitic-ferritic sample: (a) optical image and (b) critical temperature and compositional profiles.

correspond to one ferritic sample, two pearlitic-ferritic specimens and one pearlitic case, respectively. The inspection of these figures allows inferring that all the microsegregation profiles are almost constant through the paths between nodules. Plus, in Figures 8 and 9 graphite nodules are enveloped in ferrite, and T_{α} is always above T°_{p}. On the contrary, in Figures 10 and 11 nodules are surrounded by pearlite and T°_{p} overcome T_{α} from the beginning to the end of the path.

In a subsequent step, the temperature expressions published by Carazo et al. [10] were also considered for calculating the critical temperature profiles. The authors developed them using Thermocalc software and TCFE data base. However, in this instance only ferritic samples were taken into account, since the other two alloys had higher percentages of Mn and Cu, both elements not included in the formulation. One example is given in Figure 12(a) and compared with the profile obtained with Gerval and Lacaze's expressions [8], which is shown in Figure 12(b). The intersection between T_{α} and T°_{p} is almost coincident for both cases. It should be pointed out that the adoption of Carazo's formula gives a T°_{p} profile that is virtually the same from one point to the next one.

Finally, the extension of the ferrite halos were measured using the ImageJ software [11] and correlated with the following temperature intervals: T_{α}–T°_{p}, T_{α}–T_{p} and T°_{α}–T_{p}. These intervals represent the maximum temperature difference calculated for the positions along which the

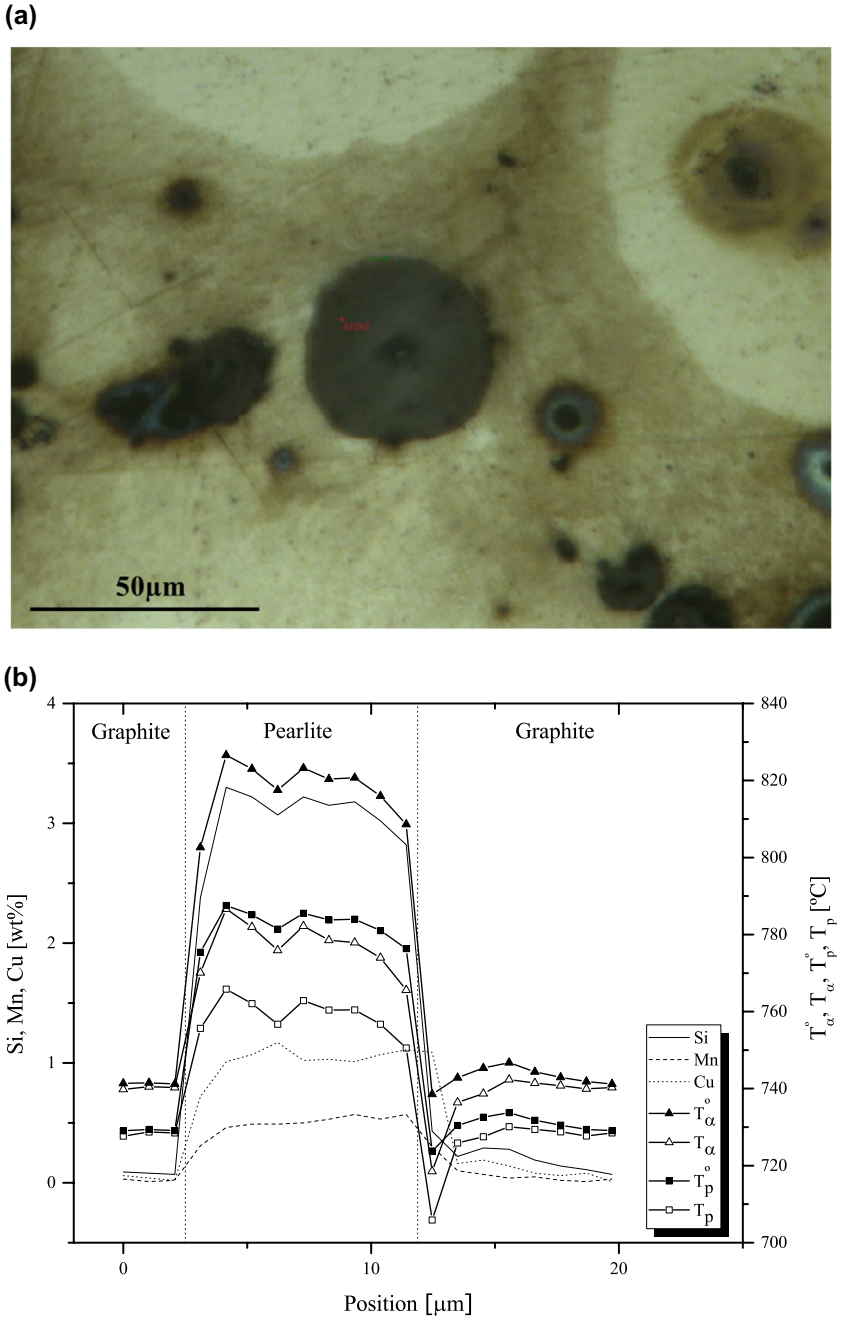

Figure 10. Pearlitic-ferritic sample: (a) optical image and (b) critical temperature and compositional profiles.

ferrite halo spreads. Results are revealed in Figure 13 for each of the analysed alloys. Ferritic cast irons present a more extended halo compared with pearlitic-ferritic and pearlitic alloys. In general, while differences in the extension of ferrite halos were registered, the intervals remain almost constant for the three types of alloys.

Discussion

As revealed by Boeri in his PhD thesis [2], changes in alloying elements' compositions when crossing ferrite/pearlite boundaries, can be associated with the solidification microsegregations. This is also in agreement with the deductions imparted by Freulon et al. who studied similar profiles observing no sudden changes in compositions through ferrite/pearlite interfaces [12]. These assessments support the fact that solid state transformations take place with no partition of alloying elements. Nevertheless, the change in the slope of the compositional profiles in Figures 5–7 would indicate that partition of the alloying elements does take place during solid state transformation, as claimed by Gou and Stefanescu

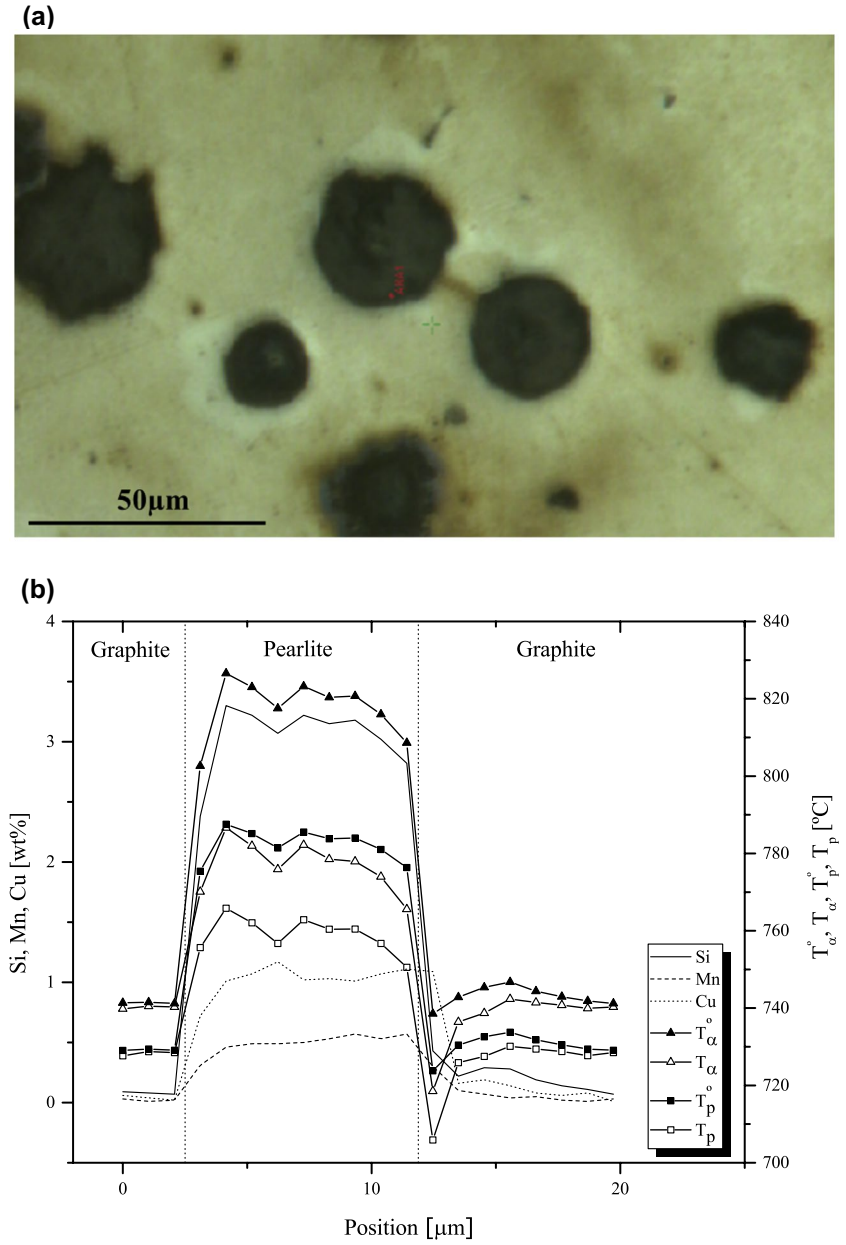

Figure 11. Pearlitic sample: (a) optical image and (b) critical temperature and compositional profiles.

[13]. This point should be checked with future experiments as it still represents a controversial topic [14,15]. In any case, these microsegregations affect the distribution of critical temperatures through the matrix.

In addition, the slope change in compositional profiles when going through ferrite/pearlite interface determinates an intersection between T_α and T_p° temperatures and consequently the transition from stable to metastable diagram. Once the temperature profiles intersect, ferrite should stop its growth, allowing pearlite growth to proceed at the ferrite/austenite interface. If those changes in slopes do not occur, no intersection between T_α and T_p° takes place and ferrite grows through the entire path between the nodules, as exemplified in Figures 8 and 9. On the other hand, if microsegregations are such that T_p° is always above $T_{\alpha'}$ no ferrite forms and only pearlite is present surrounding the nodules, as illustrated in Figures 10 and 11.

Taking into account that the three varieties of alloys were cooled to room temperature at the same rate and in light of the information given in Figure 13, it can be inferred that for continuous cooling conditions at a certain cooling rate, the available time for diffusion of *C* does not determine the extension of the halos.

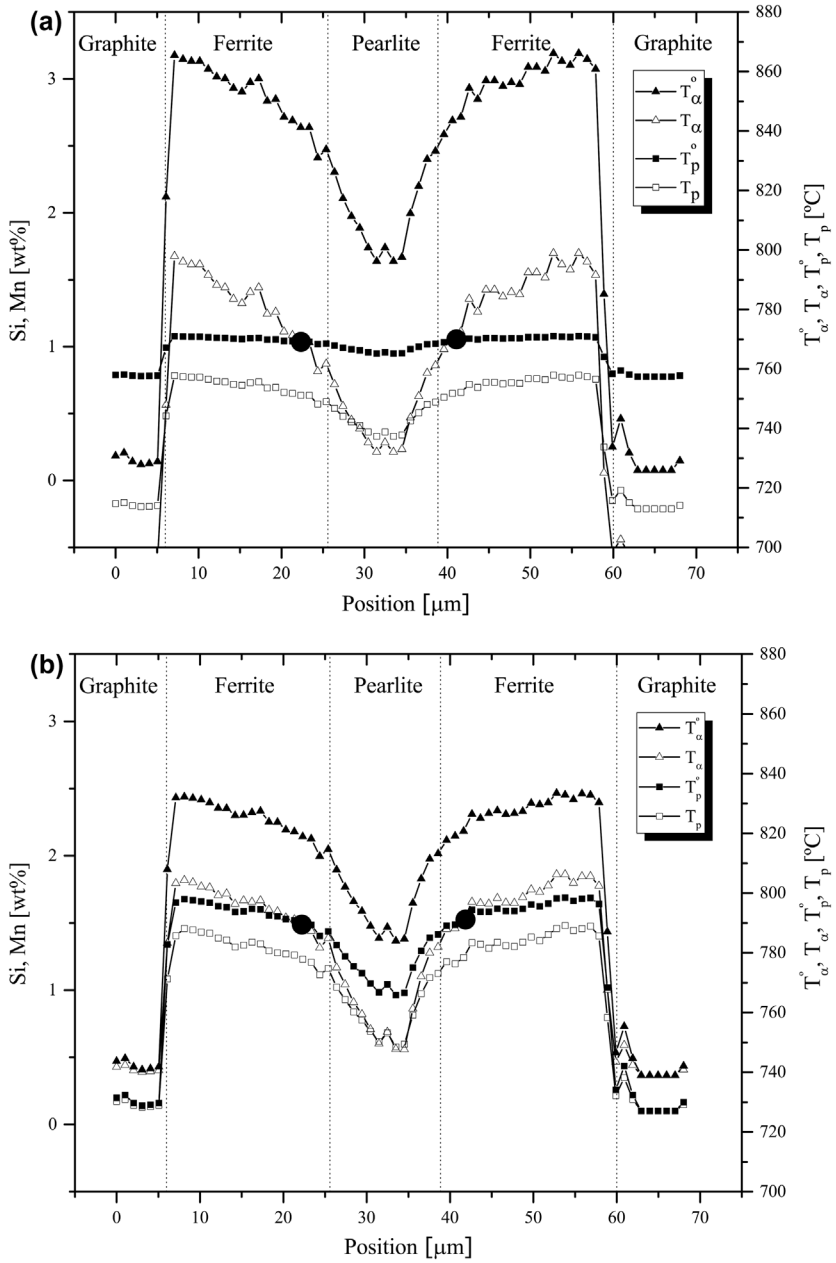

Figure 12. Critical temperature profiles for a ferritic sample: (a) as obtained making use of Carazo's formulas [10] and (b) as calculated with the Lacaze and Gerval's expressions [8].

Instead, the magnitude of their extension would be conditioned by the previously mentioned intersection between T_α and T_p°. This is valid for all the cooling rates that allow diffusional solid state transformations with no partition of substitutional elements but it is not true for those that inhibits or restrict carbon diffusion phase transformations.

The correlations between the position where T_α and T_p° converge and the position of the ferrite/pearlite interface, i.e. the ending position of the ferrite halo, are illustrated in Figure 14 for all the examined alloys. It can be inferred that there is a linear relation between these two quantities and it is reflected by the linear equation indicated in the graphic and the high value of the determination coefficient. Therefore, the ferrite halo cannot extend much further than the position at which T_α and T_p° intersect.

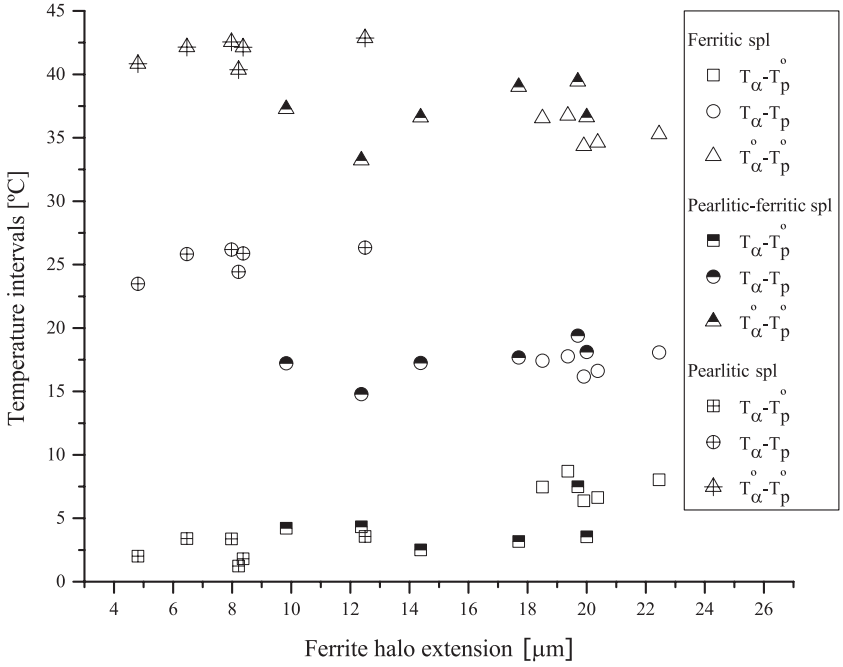

Figure 13. Correlation between the extension of the ferrite halos and several temperature intervals for all the available samples.

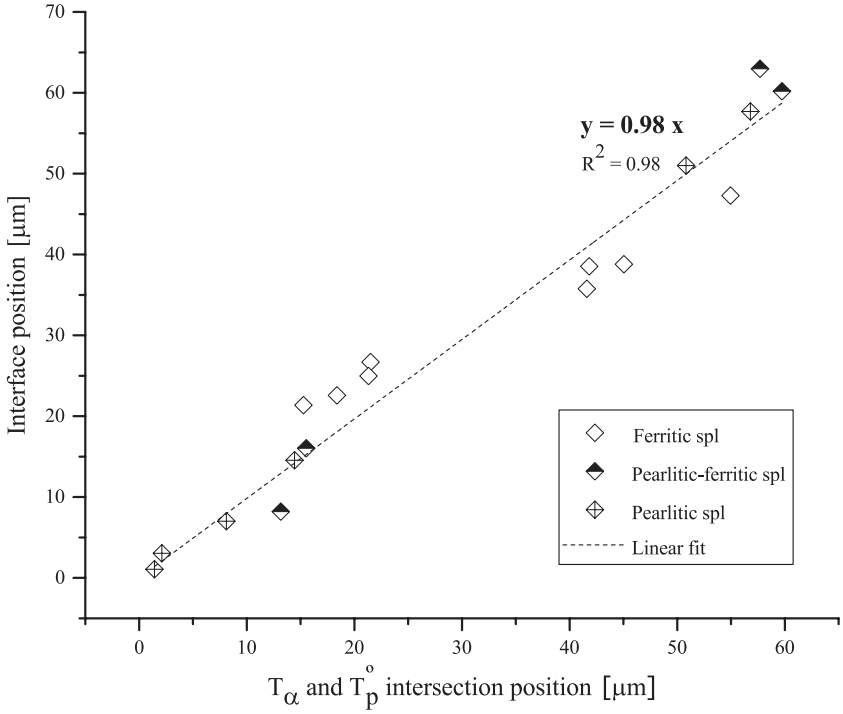

Figure 14. Correlation between the position at which T_α and T_p° intersect and the interface position.

Conclusions

The results of the present paper do confirm the current knowledge about the behaviour of microsegregations in cast irons. The smooth changes in the alloying element's profiles when going through the ferrite/pearlite boundary would indicate that microsegregations in solid state are inherited from the solidification step and that no segregation takes place during eutectoid transformations.

On the other hand, this behaviour was studied in order to arrive to new conclusions related with the extension of the ferrite halo. Assuming no partition of alloying elements during solid state transformations, the microsegregations inherited from the solidification step determines an intersection between T_α and T_p° temperatures, when these are punctually evaluated. As a result, the transition from stable to metastable system takes place and then the ferrite halo cannot further grow since pearlite nucleates at ferrite/austenite interface making way to the pearlite growth. Higher microsegregations make T_α and T_p° intersection to occur closer to the graphite nodules

and thus the ferrite halos extend shorter distances. This is valid for low enough cooling rates which are expected to allow carbon diffusion under equilibrium conditions and the development of the ferrite halo, before the temperature reaches T_p° in the last-to-freeze zones and the pearlite growth starts. If no intersection between T_α and T_p° temperatures occurs, ferrite can grow through the entire path between the graphite nodules.

It is worth noting that only one cooling rate was considered (20 K/min), so kinetics aspects were not taken into account, which represent an interesting aspect for future work.

Acknowledgements

The authors would like to thank the Sánchez and Piccioni company for allowing the authors using its facilities to carry out the casts. Laura N. García and Fernando D. Carazo are members of CONICET and would like to thank the institution for the provided economic support.

Disclosure statement

No potential conflict of interest was reported by the authors.

Funding

This work was supported by CONICET.

Notes on contributors

Laura N. García is a PhD student at Instituto de Mecánica Aplicada, Universidad Nacional de San Juan. The author's research interests are Thermodynamics; phase transformations; nodular cast irons.

Fernando D. Carazo is a professor at Universidad Nacional de San Juan and CONICET researcher. The author's research interests are phase transformations and mechanical properties in metal alloys.

Patricia M. Dardati is a professor at Universidad Tecnológica Nacional, Facultad Regional Córdoba. The author's research interests are numerical modeling; multi-scale modeling; nodular cast iron.

ORCID

Fernando D. Carazo http://orcid.org/0000-0002-2580-5337
Patricia M. Dardati http://orcid.org/0000-0002-3294-2962

References

[1] Zhou J. Colour metallography of cast iron. China Foundry. 2009; 7 (1): 76–88.
[2] Boeri R. The solidification of ductile cast iron [dissertation]. Vancouver: University of British Columbia; 1989.
[3] Lacaze J, Boudot A, Gerval V, et al. The role of manganese and copper in the eutectoid transformation of spheroidal graphite cast iron. Metall Mat Trans A. 1997;28:2015–2025.
[4] Andersson JO, Helander T, Höglund L, et al. Thermo-Calc and DICTRA, computational tools for materials science. Calphad. 2002;26:273–312.
[5] Lacaze J, Ford S, Wilson C, et al. Effects of alloying elements upon eutectoid transformation in as-cast spheroidal graphite cast irons. Scand J Metall. 1994;23: 151–163.
[6] Roviglione A. Solificación y gradientes en el líquido I: origen de la ferrita en ojo de buey ('bull eye') en hierro dúctil y fundición vermicular [Solidification and gradients into the liquid I: the origin of bull eye ferrite in ductile iron and vermicular ductile cast iron]. Suplemento de la Revista Latinoamericana de Metalurgia y Materiales. 2009;S1(3):1379–1388. Spanish.
[7] Gerval V, Siclari R, Lacaze J. Modelling continuous cooling transformation diagrams of spheroidal graphite cast irons. Int J Cast Metals Res. 1999;11:477–482.
[8] Gerval V, Lacaze J. Critical temperature range in spheroidal graphite cast irons. ISIJ Int. 2000;40:386–392.
[9] ASTM A536-84. Standard specification for ductile iron castings. West Conshohocken (PA): ASTM International; 2014. Available from: www.astm.org.
[10] Carazo FD, Dardati PM, Celentano DJ, et al. Nucleation and growth of graphite in eutectic spheroidal cast iron: modeling and testing. Metall Mat Trans A. 2016;47A:2625–2641.
[11] Schneider CA, Rasband WS, Eliceiri KW. NIH Image to ImageJ: 25 years of image analysis. Nat Methods. 2012;9:671–675.
[12] Freulon A, de Parseval P, Josse C, et al. Study of the eutectoid transformation in nodular cast irons in relation to solidification microsegregation. Metall Mat Trans A. 2016;47A(11):5362–5371.
[13] Guo X, Stefanescu DM. Partitioning of alloying elements during the eutectoid transformation of ductile iron. IJCMR. 1999;11:437–441.
[14] Freulon A, De Parseval P, Josse C, et al. Letter to the editor: regarding the paper 'Study of the eutectoid transformation in nodular cast irons in relation to solidification microsegregation'. Metall and Mat Trans A. 2016;48A:2127–2129.
[15] Freulon A, De Parseval P, Josse C, et al. Reply to the letter to the editor: Regarding the paper 'Study of the eutectoid transformation in nodular cast irons in relation to solidification microsegregation'. Metall Mat Trans A. 2017;48A:2130–2131.